J. Fluid Mech. (2007), *vol.* 587, *pp.* 395–423.
doi:10.1017/S0022112007007379 Printed in the United Kingdom

Dynamics of a sessile drop in forced vibration

BOJAN VUKASINOVIC, MARC K. SMITH AND ARI GLEZER

Woodruff School of Mechanical Engineering, Georgia Institute of Technology, Atlanta, GA 30332-0405, USA

(Received 2 September 2005 and in revised form 12 May 2007)

The interfacial dynamics of a sessile water drop was investigated experimentally. The low-viscosity drop was forced by an underlying diaphragm driven vertically by a piezoelectric actuator. This high-frequency forcing produced very low diaphragm displacements, even at high acceleration amplitudes. As the driving amplitude was increased from zero, the drop exhibited several transitions to states of increasing spatio-temporal complexity. The first state of the forced drop consisted of harmonic axisymmetric standing waves that were present for even the smallest diaphragm motion. Wave modes up to 14 were observed and compared to theoretical results. As the forcing amplitude increased above a critical value, a parametrically driven instability occurred that resulted in the appearance of subharmonic azimuthal waves along the contact line. The critical accelerations and the resulting wavenumbers of the azimuthal waves were documented. For larger values of the forcing amplitude, the subharmonic azimuthal waves coupled with the harmonic axisymmetric waves to produce a striking new lattice-like wave pattern. With a further increase in the forcing amplitude, the lattice mode disappeared and the interface evolved into a highly disordered state, dominated by subharmonic wave motion. The characteristics of the lattice and pre-ejection modes were documented with phase-locked measurements and spectral analysis. Finally, as the forcing amplitude increased above another critical value, the interface broke up via droplet ejection from individual wave crests.

1. Introduction

The behaviour of drops, bubbles and interfaces undergoing free and forced vibrations is a problem of great practical, scientific and technological interest. Liquid drops vibrate during spray cooling and coating, atomization, ink-jet printing and fuel injection. James *et al.* (2003*a*) used 1 kHz forced vibrations to atomize rapidly small liquid drops for use in cooling discrete microelectronic circuits. Raindrops falling on a liquid/air interface can produce bubbles that vibrate to create the underwater sound of rain (Prosperetti & Oguz 1993). Bubble oscillations have also been explored as the mechanism for sonoluminescence (Crum & Roy 1994). A wide variety of gravity/capillary wave patterns have been observed on interfaces, going back to Faraday (1831). The enormous body of literature that has been generated since then is largely due to a more general interest in the physics and mathematics of pattern formation. Faraday waves take place in a simple physical system that can be used for experimental exploration and verification of mathematical theories.

Free and forced oscillations of unsupported drops have been studied since the nineteenth century. In his pioneering work, Rayleigh (1879) investigated infinitesimal-amplitude oscillations of an inviscid incompressible drop. He showed that there

were an infinite number of discrete fundamental modes (each one described in terms of a Legendre polynomial) and calculated the corresponding fundamental frequencies. Prosperetti (1980) included the effect of viscosity in his study of small-amplitude oscillations of free drops and bubbles. He concluded that the motion consists of modulated damped oscillations, where the frequency of each damped mode asymptotically approaches the inviscid normal-mode result as the damping parameter goes to zero. Trinh, Zwern, & Wang (1982) analysed experimentally the dynamics of small-amplitude shape oscillations in acoustically levitated drops. Following this work, Trinh & Wang (1982) quantified some nonlinear aspects of large-amplitude, free and driven, drop-shaped oscillations. Their work revealed that the drop has internal circulation even at relatively low oscillation amplitudes. These authors also reported that large-amplitude oscillations could break up the drop into two droplets. Tsamopoulos & Brown (1983) analysed moderate-amplitude axisymmetric oscillations of inviscid drops and bubbles and showed that the frequency of oscillation decreased as the square of the forcing amplitude increased. Lundgren & Mansour (1988) extended the previous investigations of free drops to large-amplitude nonlinear oscillations in a microgravity environment. In their numerical investigation, they found that large-amplitude oscillations could lead to states that would most likely precede drop breakup. Basaran (1992) used a finite-element simulation to examine the fundamental modes of free, viscous drop oscillations at moderate to large amplitudes. Lee, Anilkumar & Wang (1991) investigated the static shape and instability of an acoustically levitated, low-viscosity drop, and examined the large-amplitude drop deformations that ultimately lead to drop disintegration. In one example relevant to the present work, the drop was forced by direct contact with the acoustic membrane instead of the acoustic field.

In contrast to oscillating isolated drops, oscillating supported drops, and particularly their forced oscillations, have not drawn much attention until recently. The first investigation of a forced supported drop was reported by Rodot, Bisch & Lasek (1979) exactly a century after Rayleigh's work. Their experimental study was motivated by crystal growth in space and focused on the behaviour of liquid spheres in contact with solid surfaces in simulated microgravity conditions. The shape, frequency and amplitude of liquid-sphere oscillations were determined as a function of the sphere and solid–liquid surface dimension, forcing parameters and fluid viscosity. Strani & Sabetta (1984) examined theoretically the infinitesimal-amplitude oscillations of inviscid supported drops surrounded by an inviscid fluid. To solve the problem analytically, they considered a spherical drop and modelled the support by immobilizing an axisymmetric portion of the interface. They discovered that such supported drops have an additional mode that is dominated by the Legendre function P_1. This mode represents the displacement of the drop centre of mass along the axis of symmetry. Such motions are not possible for an isolated drop because of momentum considerations. Thus, the motion of a supported drop is fundamentally different from that of an isolated drop. Strani & Sabetta (1988) extended their previous work to account for the effect of finite viscosity.

Siekmann & Schilling (1989) performed a numerical investigation of the free vibration of isolated and supported inviscid liquid drops in a low-gravity environment. Their results agreed almost perfectly with those of Strani & Sabetta (1984), but deviated considerably from the experimental results of Rodot *et al.* (1979) as the drop departed further from the free state. Gañán & Barrero (1990) numerically and experimentally investigated the small-amplitude free oscillation of inviscid captive liquid drops, bridges and bubbles surrounded by a liquid or a gas under gravity. They

showed that resonance frequencies for a drop with a planar support were always lower than with a spherical support provided the drop was smaller than half a sphere. Basaran & DePaoli (1994) examined numerically the roles of fluid properties, gravity, drop volume and initial deformation in the nonlinear oscillations of pendant drops supported on a solid rod and released from an initial static deformation. Their results demonstrated the importance of the boundary layer on the rod surface in the drop dynamics. DePaoli *et al.* (1995) employed a sweep procedure and experimentally detected a hysteretic response in the case of drops pendent from the tip of a capillary tube. They confirmed that two stable oscillatory states are possible at the same value of the forcing frequency. Wilkes & Basaran (1997) studied arbitrary amplitude, forced axisymmetric oscillations of a viscous pendent or sessile liquid drop with a fixed contact line. They established the governing set of parameters for forced supported-drop oscillations and discussed their relative importance. Wilkes & Basaran (1999) analysed previous experimental observations by solving the full transient Navier–Stokes equations and using a sweep procedure in either frequency or amplitude. They showed that even low-amplitude forcing was sufficient for the onset of hysteresis.

James, Smith & Glezer (2003*b*) developed an axisymmetric Navier–Stokes solver to simulate the low-frequency dynamics of a forced sessile drop. Their simulation was able to capture the interfacial breakup and ejection of a small droplet. Range, Smith & Glezer (1998) conducted the corresponding experimental work on the mode shapes of the forced drop and the breakup mechanism for the case of low-mode excitation. In contrast, James *et al.* (2003*a*) focused on rapid drop atomization and reported that a sessile drop placed on a diaphragm vibrating near 1 kHz undergoes a hierarchy of instability modes prior to ultimate atomization. Noblin, Buguin & Brochard-Wyart (2004) investigated forced sessile drop dynamics with an emphasis on the transition from a pinned to an oscillating contact line that occurs above a critical acceleration when contact-angle hysteresis is overcome. Noblin, Buguin & Brochard-Wyart (2005) examined the behaviour of the oscillating contact line during vertical vibration of large liquid drops (puddles). They focused on the inertial regime where the contact line becomes unstable to wave-like modes of oscillation called triplons. Lyubimov, Lyubimova & Shklyaev (2006) reported a theoretical analysis of natural and forced oscillations of a hemispherical inviscid drop with an emphasis on contact-line dynamics. Their work also included results with a pinned circular contact line.

Sessile drops vibrating at high frequencies exhibit dynamics that may be related to the interfacial dynamics, wave patterns and complex mode interactions seen in liquid layers vibrated from below, i.e. Faraday waves. Faraday waves have been investigated in a number of experiments (e.g. Simonelli & Gollub 1989; Douady 1990; Edwards & Fauve 1994; Gluckman, Arnold & Gollub 1995). The large body of work on Faraday wave experiments has been reviewed by Miles & Henderson (1990) and Perlin & Schultz (2000). A review by Gollub & Langer (1999) focused on pattern formation in a liquid layer and included Faraday wave patterns.

As mentioned above, James *et al.* (2003*a*) observed several instability modes in a sessile drop on a vertically vibrating diaphragm. The present paper explores these instability modes in more detail. In the next section, the experimental procedure is described. Section 3 presents visualizations of the four distinct modes that were observed in the drop. Data that characterize each mode are presented and discussed. The phase dynamics of some of this data is presented in § 4 to provide a low-dimensional description of the drop dynamics. A final discussion and some conclusions are given in § 5.

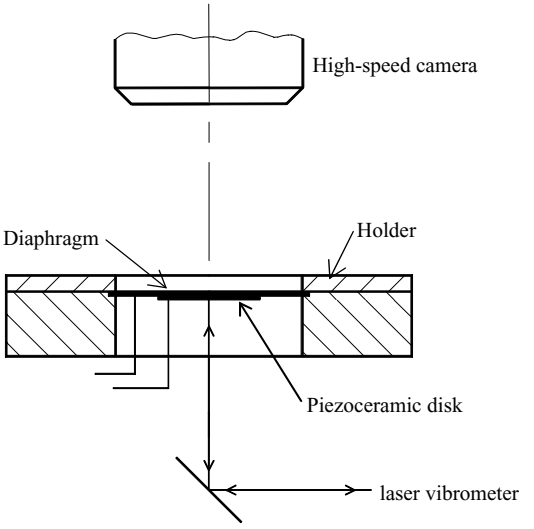

FIGURE 1. Experimental set-up.

2. Experimental procedure

The present work focused on the evolution of the interfacial motion of a sessile drop vibrated vertically using high-frequency (~1 kHz) low-amplitude external forcing. The experimental set-up is presented in figure 1. The actuator used for the drop forcing was a thin circular iron–nickel diaphragm (0.1 mm thick) with a thin piezoceramic disk (PZT5, 19.7 mm diameter, 0.12 mm thickness) bonded to its bottom surface. The diaphragm was clamped around its circumference by an aluminium holder so that its active diameter was 30 mm. A sinusoidal voltage signal applied to the piezoceramic disk caused it to expand and contract, producing a sinusoidal vertical vibration of the diaphragm. A sessile water drop placed at the centre of the top surface of the diaphragm was forced by this vibration. More details on the actuator design and auxiliary hardware are discussed by Vukasinovic (2002).

The diagnostics used in the present experiments included simultaneous high-speed digital video imaging of the forced drop (uniformly illuminated by a ring light source) and optical measurement of the displacement and velocity at the centre of the diaphragm using a Polytec optical vibrometer. The laser beam of the vibrometer was focused on the bottom centre of the actuator and surface motion was detected remotely using an interferometric technique. An Eppendorf micro-pipette was used to place a liquid drop of specified volume at the centre of the upper surface of the diaphragm in all experiments. Drop volumes of 10, 25, 50, 75 and 100 μl were used in this work. The entire experimental set-up was built on an optical table for isolation from ambient vibrations. The actuator assembly was protected from air motion within the room and its temperature was monitored by an attached thermocouple.

The mode shape of the dry diaphragm vibration was characterized using the laser vibrometer. The basic motion was first visualized using a surface distribution of fine-grain powder (visualization not shown), which revealed only a single axisymmetric mode of vibration. Next, the surface velocity was measured phase-locked to the driving signal at four azimuthal points at the same radius and then along the diameter of the diaphragm at 30 equally spaced points 1 mm apart. The actuator assembly was

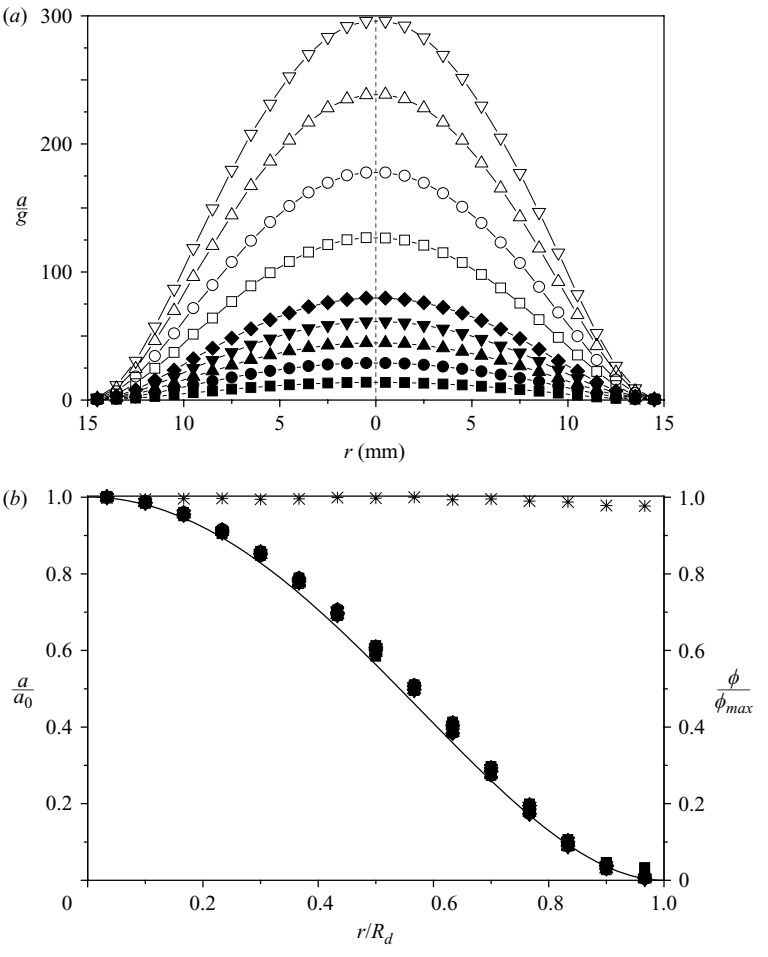

FIGURE 2. The radial distributions of: (*a*) diaphragm acceleration at nine forcing levels with $f_d = 1$ kHz, and (*b*) the corresponding normalized acceleration (symbols) and phase (*). For reference, the solid line is $a/a_0 = (1 - (r/R_d)^2)^2$, which is the functional form for the approximated first mode shape of a clamped circular plate from Leissa & Chern (1992).

traversed relative to the fixed laser beam along a given diameter using a stepper-motor-controlled horizontal traversing mechanism with a resolution of 3 μm. At each radial location, the surface velocity was recorded over 1000 driving periods, i.e. about 1 s.

The time-averaged radial distributions of the diaphragm surface acceleration for nine different driving amplitudes are shown in figure 2(*a*). Figure 2(*b*) shows that the phase of the surface motion, ϕ, derived from the phase-locked measurements was uniform along the diameter. Thus, the diaphragm motion was indeed axisymmetric over this range of driving amplitudes. Figure 2(*b*) also shows that the acceleration distributions at the various driving amplitudes scale with the centreline acceleration a_0 and collapse onto a single curve. Leissa & Chern (1992) examined the forced vibration of a uniform circular clamped plate at frequencies close to the resonance frequency and showed that the approximate solution, $a/a_0 = [1 - (r/R_d)^2]^2$, where R_d is the active radius, describes the first-mode shape of the plate to within 5 %. The experimental results are close to this approximate solution, as shown by the solid line in figure 2(*b*). This result showed that the surface acceleration of the diaphragm could

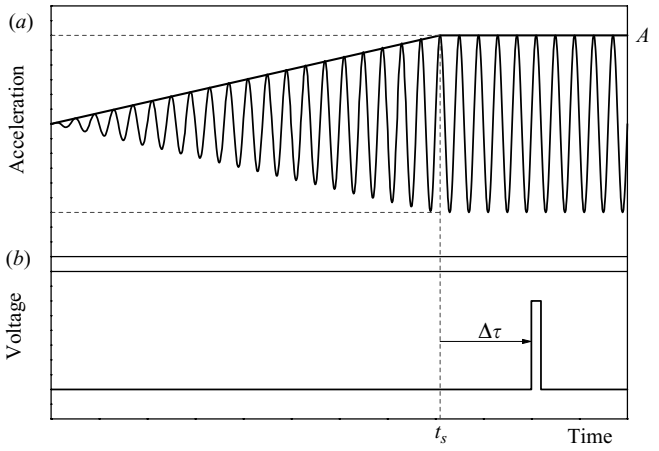

FIGURE 3. (*a*) The ramped-amplitude actuator signal (A is the amplitude at time t_s), and (*b*) the time delay $\Delta\tau$ for the data acquisition trigger.

be characterized by a single acceleration measurement. Therefore, all accelerations reported in the remainder of this paper were measured at the centre of the diaphragm and the subscript notation is omitted.

It should be noted that in earlier experimental investigations of supported drop vibrations (e.g. Rodot *et al.* 1979; DePaoli *et al.* 1995; Range *et al.* 1998), forcing was applied using an electromagnetic shaker, typical operating frequencies were no larger than about 300 Hz, and acceleration amplitudes were less than $15g$. In the present experiments, acceleration amplitudes could be as high as $1000g$ at frequencies of the order of 1 kHz. However, in contrast to these earlier investigations, the acceleration felt by a liquid drop on the top surface of the diaphragm has a significant radial variation, i.e. the acceleration has a maximum at the centre and decreases toward the edge of the diaphragm (see figure 2). For example, in a 100 µl drop with a nominal radius of $0.29\,R_d$, the acceleration varies along the radius of the drop by approximately 15 % between the centreline and the drop contact line. The disadvantage of this acceleration non-uniformity is balanced by the large domain of frequency and acceleration amplitude over which forced drop instabilities can be investigated and by the ability of the system to rapidly atomize the drop, as discussed by James *et al.* (2003*a*).

To avoid transient effects and to allow enough time for the instability modes to fully develop, the experiments reported here were performed with amplitudes of the forcing signal linearly ramped in time. The time-harmonic driving waveform was generated by a digital/analogue (D/A) board in a laboratory computer. The amplitude of the driving signal was increased linearly in time to a predetermined diaphragm acceleration level A and thereafter held constant, as shown schematically in figure 3. The slew rate α (or the ramping time $t_s = A/\alpha$) of the driving signal and the time delay $\Delta\tau$ for the data acquisition trigger were varied independently. The ramping time was taken to be an integer multiple N of the actuator forcing period T (i.e. $t_s = N/f_d$, where f_d is the forcing frequency). In all experiments, choosing $N > 100$ adequately reduced the transient effects of the ramp modulation. Before amplification of the driving signal, the D/A output was low-pass filtered to minimize the presence of any higher harmonics that resulted from the digital to analogue signal conversion process.

The measurements of James *et al.* (2003*a*) showed that the acceleration of the centre of the diaphragm was weakly nonlinear with respect to the applied voltage when the acceleration level was near $200g$. To minimize these nonlinear effects, all experimental measurements reported here were performed at peak acceleration amplitudes substantially lower than $200g$ when operating at off-resonance frequencies.

A typical method used to characterize the interfacial dynamics of a drop involves an analysis of the time traces of the drop interfacial displacement in response to external forcing. One way to measure the amplitude of interfacial waves is to use a laser beam propagating through the fluid from below and measure the position of the refracted beam by a position-sensing photodiode (e.g. Mesquita, Kane & Gollub 1992). This method works well when the light-detecting sensor and light source are located on opposite sides of the liquid (e.g. Christiansen, Alstrøm & Levinsen 1995). When this is not possible, the source and the sensor must be located on the same side of the liquid (e.g. Douady 1990; Besson, Edwards & Tuckerman 1996).

Uniform surface illumination and video imaging can be used to measure surface displacement, but it has the disadvantage that there is no clear relationship between the collected light intensity and the interfacial displacement. However, in the absence of a preferred direction in the illumination, it may be assumed that a light intensity map is a true representation of the surface wave pattern. This latter approach was the technique adopted in the present work.

A ring light source was used to uniformly illuminate the drop interface. The reflected light from the drop was recorded by a high-speed camera at 10 000 f.p.s. This frame rate provided good time resolution for the measurements, but it restricted the field of view to just a fraction of the drop. The intensity time-history $I(t)$ was sampled for 2^{13} (=8192) frames starting at $t_s + \Delta\tau$. The time delay $\Delta\tau$ that was used ensured that the interfacial mode shape was fully established at the prescribed driving amplitude. Since the illumination was uniform, it was assumed that the image recorded by the camera was related to the interface shape as long as the light intensity was within the camera's 8-bit dynamic range.

The independent external parameters governing the interfacial dynamics of a forced drop are the driving frequency f_d, acceleration a, and slew rate α; the drop volume V and contact angle θ; the fluid viscosity μ, density ρ, and surface tension σ; and gravity g. The slew rate is important only when it is so large that there is not enough time for the interfacial modes on the drop to become fully developed. This effect was suppressed in the present results by the experimental procedure. For reference, dimensional parameters (and the dimensionless parameters discussed next) for the five drop volumes used in this work are given in table 1.

Dimensionless parameters were formed using the radius of curvature R of a spherical-cap drop with the given volume and contact angle and the inviscid capillary time scale $\sqrt{\rho R^3/\sigma}$. Thus, the relevant dimensionless parameters used in this work to describe the evolution of a forced supported drop are the diaphragm acceleration $a^* = \rho R^2 a/\sigma$ and driving frequency $\omega_d^* = 2\pi f_d \sqrt{\rho R^3/\sigma}$, the drop volume $V^* = V/R^3$, and the contact angle θ. Viscous effects are measured by the Reynolds number, defined as $Re = \sqrt{\rho\sigma R}/\mu$. The smallest Reynolds number in this work was $Re = 313$ and that was for the smallest drop. Wilkes & Basaran (1997) showed that viscous effects were negligible in a supported drop for $Re > 20$. Thus, the use of inviscid scales is appropriate.

Gravitational body forces compared to surface tension forces are measured by the gravity number $G = \rho R^2 g/\sigma$ which varied from 0.40 to 2.02 in this work. These values suggest that gravity effects could be important, especially at the largest drop

Measured drop parameters			Computed drop parameters: Static drop with gravity	Computed drop parameters: Spherical-cap drop (no gravity)		Dimensionless drop parameters	
Drop volume V(μl)	Contact angle θ (deg.)	Contact radius R_c (mm)	Contact radius R_c (mm)	Contact radius R_c (mm)	Radius of curvature R (mm)	Drop volume V^*	Gravity number G
10	88	1.66	1.76	1.71	1.71	1.98	0.40
25	87	2.42	2.46	2.35	2.35	1.93	0.76
50	86	3.24	3.19	2.98	2.99	1.88	1.22
75	85	3.70	3.74	3.44	3.45	1.82	1.63
100	84	4.12	4.20	3.82	3.84	1.77	2.02

Physical properties of water		
Density, ρ	Viscosity, ν	Surface tension, σ
998 $\mathrm{kg\,m^{-3}}$	$1.12 \times 10^{-6}\ \mathrm{m^2\,s^{-1}}$	$71.4 \times 10^{-3}\ \mathrm{kg\,s^{-2}}$

TABLE 1. Dimensional and dimensionless drop and fluid parameters.

volume. A static drop flattens and spreads out under gravity. Standard capillary shape computations for the largest drop size in this work show that the contact radius of the drop with gravity is 10 % larger than the contact radius of a spherical-cap drop with the same volume and contact angle (without gravity). The measured contact radii for all the drops examined in this work were within 2 % of the computed contact radii for the drop with gravity, except for the smallest drop, which was 6 % smaller. Thus, gravity caused the drops to spread out by at most 10 %. However, this change in the drop shape and any other gravity effects did not seem to affect the dynamical motion of the drop observed in this work.

The comprehensive characterization of the drop dynamics over the full range of driving accelerations and frequencies as presented in this work was only done for the largest drop size $V = 100\,\mu\mathrm{l}$ ($V^* = 1.77$). These results were supplemented with additional measurements on four smaller drops (see table 1 for values) for two instances (figures 7 and 11).

3. Interfacial wave patterns of the forced drop

3.1. *General overview*

Several interfacial wave patterns in a forced sessile drop as the forcing amplitude was increased from zero are shown in the sequence of side-view, high-speed images (500 f.p.s.) in figure 4. The forcing frequency was 1040 Hz (the linear resonance frequency of the coupled drop/diaphragm system was 980 Hz) and the slew rate of the forcing signal was $50g\ \mathrm{s^{-1}}$ ($0.048\,g$/driving period). The unforced water drop (100 μl) is shown for reference in figure 4(*a*). Axisymmetric standing waves appeared on the interface (figure 4*b*). These axisymmetric waves were present even at the lowest forcing amplitude used in this study ($\sim 0.5\,g$). This motion is a basic mode shape of oscillation for a supported drop.

At larger forcing amplitudes, an azimuthal instability of the basic mode shape appeared along the contact line of the drop resulting in a loss of the axial symmetry

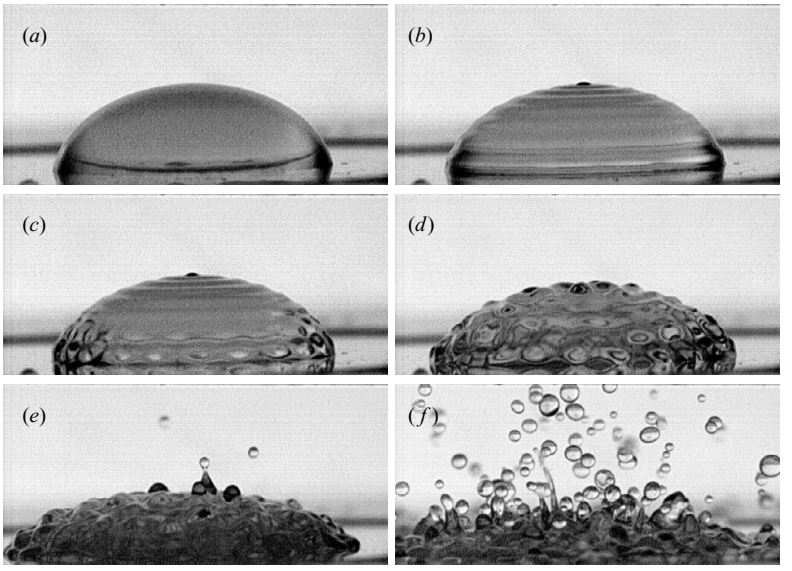

FIGURE 4. Motion in a 100 µl drop ($V^* = 1.77$) with slowly ramped forcing at $\omega_d^* = 183.8$: (*a*) unforced, (*b*) axisymmetric waves ($a^* = 30.3$), (*c*) coupling of axisymmetric and azimuthal waves ($a^* = 56.6$), (*d*) pre-ejection state ($a^* = 323.3$), (*e*) ejection onset ($a^* = 351.6$), and (*f*) atomization ($a^* = 371.8$).

of the interfacial shape (figure 4*c*). For a given fluid and drop volume, the threshold amplitude of this azimuthal instability increased with increasing driving frequency and decreased with increasing slew rate of the driving signal. Further increases in the forcing amplitude resulted in an increase in the amplitude and spatial complexity of the interfacial waves (figure 4*d*). Eventually, the interfacial wave motion became intense enough to result in the ejection of secondary droplets from the wave crests (figure 4*e*). It is noteworthy that when droplet ejection occurred, the amplitude of the wave motion on the entire interface of the primary drop was approximately uniform and the ejection sites were uniformly distributed (determined by visual inspection). Shortly after the onset of droplet ejection, the process accelerated rapidly and the primary drop completely atomized (figure 4*f*) over a time interval of about 0.3 s (300 T).

The main interest of the present paper is the sequence of instabilities exhibited by the primary sessile drop as it was forced over a range of forcing amplitudes from 0g–135g, which takes the drop from rest to the pre-ejection mode. A closer inspection of the resulting wave patterns are shown in a sequence of top-view high-speed (1000 f.p.s.) video images in figure 5. The forcing amplitude slew rate for this sequence was $12g\ \mathrm{s}^{-1}$(0.013g/driving period). The axisymmetric basic mode shape is shown in figure 5(*a*). The azimuthal instability was triggered along the contact line when the forcing amplitude was 18g–22g (figure 5*b*). The azimuthal motion spread across the entire interface of the drop as the forcing amplitude increased (figure 5*c*). For forcing amplitudes near 34g–38g, the interface wave pattern changed to one with a well-defined sixfold symmetry (figure 5*d*). This wave pattern, called the lattice mode, has five azimuthal rings at different radii with each ring shifted azimuthally by $\pi/6$ relative to the adjacent ring. When the forcing amplitude was 55g–60g, the sixfold symmetry of the waves in each ring appeared to be replaced by azimuthal waves with a higher wavenumber (figure 5*e*). Finally, when the forcing amplitude was 130g–135g,

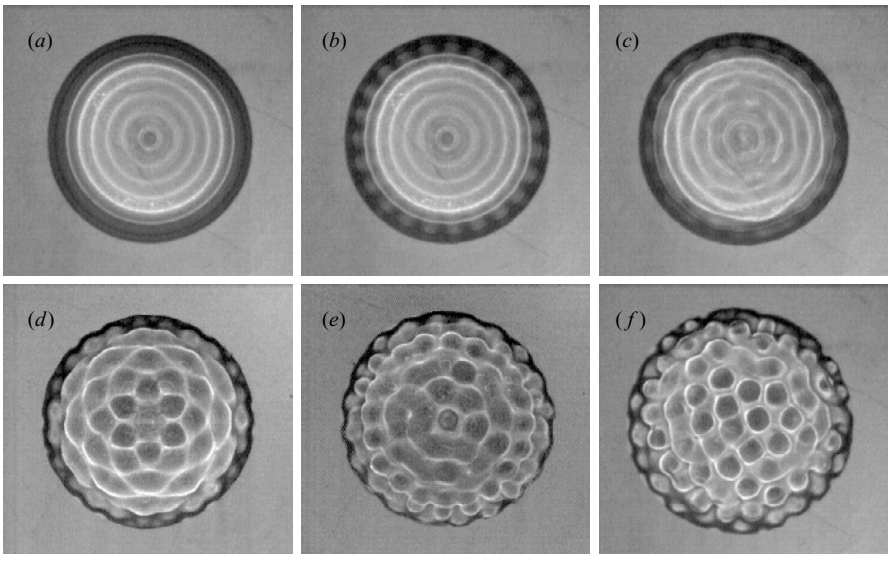

FIGURE 5. Motion in a 100 µl drop ($V^* = 1.77$) with slowly ramped forcing at $\omega_d^* = 159.6$: (*a*) axisymmetric waves ($a^* = 33.2$), (*b*) just above the onset of azimuthal waves ($a^* = 42.0$), (*c*) full axisymmetric breakdown ($a^* = 56.0$), (*d*) lattice mode ($a^* = 77.8$), (*e*) lattice breakdown ($a^* = 115.2$), and (*f*) the pre-ejection mode ($a^* = 271.8$).

the entire interface was covered by a random distribution of wave cells that preceded droplet ejection (Figure 5*f*). The acceleration thresholds of the various instabilities increased with increasing driving frequency.

It is noteworthy that the interface (and internal) motions associated with these instabilities resulted in radial spreading of the primary drop. This effect was most pronounced at high forcing levels. For example, the difference between figures 5(*a*) and 5(*f*) show that the nominal diameter of the drop (as measured by the outer dark band) increased by 12 % over the time the drop was forced to the pre-ejection state. Radial expansion of the contact line is also evident between figures 4(*a*) and 4(*e*).

These results show that a forced sessile drop exhibits four distinct wave patterns, namely, axisymmetric standing waves, azimuthal waves, the lattice mode, and pre-ejection waves, each separated by a transition. In the remainder of this section, detailed measurements of each wave pattern and their associated transitions are presented.

3.2. *Axisymmetric standing waves*

The high driving frequencies used in this study enabled much higher axisymmetric modes to occur in the drop than in earlier investigations (e.g. Rodot *et al.* 1979; DePaoli *et al.* 1995; Range *et al.* 1998). Most of this previous work examined the first few low-order mode shapes of the drop with frequencies no larger than 300 Hz. The low viscosity of the liquid used in the present work reduced wave damping in the drop so that the higher modes with frequencies of the order of 1 kHz were easily sustained at observable amplitudes.

The mode number m of each axisymmetric mode of oscillation of the drop and the corresponding resonance frequency f_m were measured using the following process. The frequency of the forcing signal was set to its highest value within the nominal operating range of 0–1000 Hz and the amplitude of the signal was set to its smallest possible value, which corresponded to an acceleration of $0.5g$. The frequency of

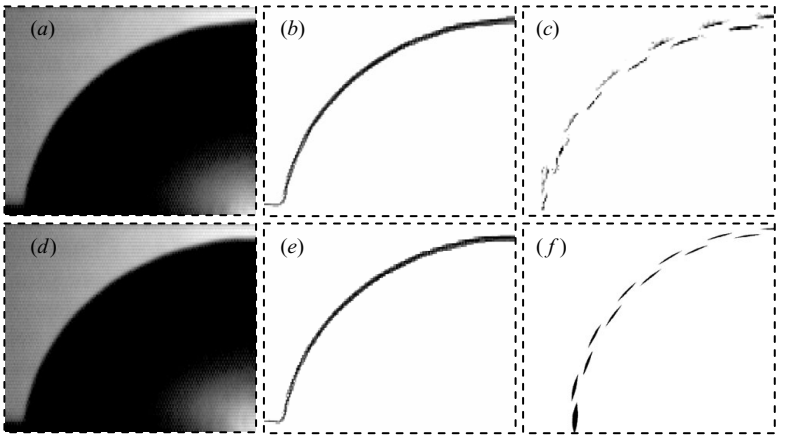

FIGURE 6. Detection of the axisymmetric mode number m ($V^* = 1.77$, $a^* = 1.0$): (a, d) raw images of the drop half-profiles with a 180° phase difference, (b, e) the corresponding drop interfaces, and (c) inverted image of subtracted interfaces showing the mode number $m = 11$. Image (f) is a subtracted interfaces image from a computer-generated drop mode $m = 11$.

the forcing signal was then decreased at a rate of $2\,\mathrm{Hz\,s^{-1}}$ while the acceleration amplitude at the centre of the diaphragm was held fixed using a feedback control loop. Simultaneously, a side view of the drop was recorded (orthogonal to a central meridian plane of the drop) using high-speed video with back illumination. This illumination resulted in a liquid–air interface with sharp contrast (see figures 6a, d). The interface was extracted from individual drop images using the Sobel edge-detection algorithm (e.g. Pratt 1978). In the absence of forcing, this edge-detection procedure yielded interface shapes for static drops that matched numerically determined shapes for the different drop volumes used in this study (Vukasinovic 2002). These static shapes also showed that the drop contact angle θ varied between 84° and 88° and was biased toward larger values for smaller drops.

As the driving frequency decreased, the drop passed through a series of axisymmetric resonance modes. The corresponding resonance frequency f_m was determined by finding the maximum magnitude of the interface oscillation through visual inspection. The error in this measurement was approximately $\pm 3\,\%$.

For each axisymmetric mode, the corresponding mode number m is defined by the number of node points on half the drop, i.e. the number of intersections between the interface images of a forced and an unforced drop at half its profile (e.g. Wilkes & Basaran 1997; Strani & Sabetta 1984). Because the interface displacements in this investigation were extremely small, two interface images of the forced drop at extremes of its motion and exactly opposite in phase were used (figures 6b and 6e, respectively). These interface images were subtracted and the resultant image inverted to give the image shown in figure 6(c). The mode number is equal to the number of individual gaps in this image; in this case $m = 11$. Figure 6(f) is an idealized version of the inverted and subtracted image in figure 6(c) from a computer-generated drop mode $m = 11$ that clearly shows the gaps that define the mode number m.

The axisymmetric standing waves in the present study were induced even at the lowest possible acceleration amplitude for this actuator system ($5\,\mathrm{m\,s^{-2}}$), which was based on the highest forcing frequency ($\sim 1\,\mathrm{kHz}$) and the smallest diaphragm displacement amplitude ($\sim 1\,\mu\mathrm{m}$) that was used. Despite this substantial minimum

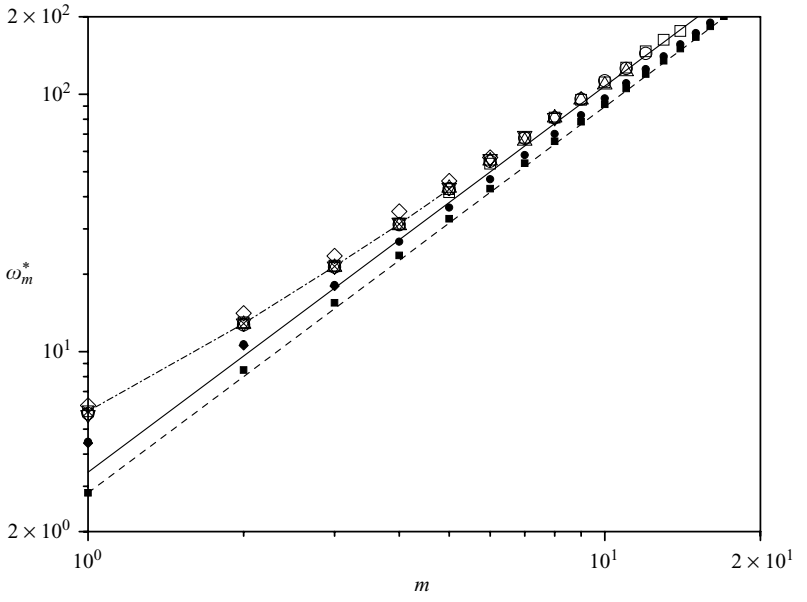

FIGURE 7. The dimensionless resonance frequency ω_m^* versus the mode number m for axisymmetric standing waves with drop volumes $V^* = 1.77$ (□), 1.82 (○), 1.88 (Δ), 1.93 (∇) and 1.98 (◇). See table 1 for other drop parameters. The other experimental and theoretical data are: Noblin *et al.* (2004) (– — ⊠ – —), the experimental asymptote $\omega_m^* \sim m^{3/2}$ (—), Strani & Sabetta (1984) (●), free half-drop oscillations (■), pinned half-drop oscillations from Lyubimov *et al.* 2006 (◆), and the theoretical asymptote $\omega_m^* = \sqrt{8}m^{3/2}$ (- - -).

acceleration amplitude, the onset threshold for axisymmetric waves in the forced drop is most probably zero since this is the expected behaviour of a single-degree-of-freedom system in the limit of small forcing amplitude, i.e. a spring-mass-damper system in resonance.

The diaphragm oscillation displacement amplitude was at least three orders of magnitude smaller than the drop radius, so nonlinear effects in the axisymmetric motion of the drop were negligible. Also, the Reynolds number $Re > 310$ for these experiments, so viscous effects were negligible. Thus, it is reasonable to assume that the measured resonance frequencies are equal to the natural frequencies ω_m of an inviscid sessile drop. The natural frequencies of an inviscid drop supported by a planar surface with a fixed contact line depend only on the drop geometry (radius of curvature R of the equivalent spherical-cap drop and contact angle θ), fluid properties (surface tension σ and density ρ), gravity g, and mode number m. In dimensionless form, this is

$$\omega_m^* = \omega_m \sqrt{\rho R^3/\sigma} = func(m,\ \theta,\ G), \tag{1}$$

where the gravity number $G = \rho R^2 g/\sigma$.

The dimensionless frequency ω_m^* versus the mode number m for axisymmetric drop motion is plotted in figure 7 for five drop volumes (10, 25, 50, 75 and 100 µl). See table 1 for other relevant drop parameters. The measured data have collapsed to a single curve whose large-wavenumber asymptote is the power law $\omega_m^* \sim m^{3/2}$. The collapse of the data shows that variations in shape due to gravitational spreading are not important with respect to this axisymmetric motion for this parameter range.

Mode	ω_m (rad s^{-1})	ω_m^{NBBW} (rad s^{-1})	Relative difference (%)
1	213.6	205.5	−3.8
2	465.0	451.1	−3.0
3	772.8	752.7	−2.6
4	1124.7	1097.7	−2.4
5	1489.1	1499.2	0.7

TABLE 2. Resonance frequencies of the first five axisymmetric modes for a 100 µl water drop measured in the current work (ω_m) and in the work of Noblin *et al.* (2004) (ω_m^{NBBW}) and the relative difference.

Note that for these measurements, the video images showed that the contact line of each drop appeared to be pinned to the surface of the diaphragm.

The measured resonance frequencies from Noblin *et al.* (2004) for the first five axisymmetric modes of a pinned water drop with a volume of 100 µl and an equilibrium contact angle $\theta = 84^\circ$ are also plotted in figure 7 and given in table 2. Note that the mode number m in the present work corresponds to Noblin *et al.*'s mode $m+1$. The agreement between these experiments and ours is good, differing from each other by at most 4 %.

Lamb (1932) analysed a spherical free drop undergoing inviscid incompressible infinitesimal-amplitude axisymmetric oscillations within an inviscid external fluid of density ρ_e. His result for the natural frequencies is

$$\omega_m^* = \sqrt{\frac{(m-1)m(m+1)(m+2)}{m+1+m\rho_e/\rho}}. \tag{2}$$

The even modes of oscillation of the full free drop are symmetric about the equator of the sphere and so they represent the oscillation of a hemispherical drop on a planar surface with a mobile contact line and a fixed contact angle of 90°. Numbering these even modes as $m/2 \to m$ for $m = 2, 4, \ldots$, gives the filled square symbols in figure 7. These data are below the experimental data because the contact line of the drop is mobile, not pinned.

Strani & Sabetta (1984) computed the natural frequencies of a supported drop by considering a liquid sphere with a lower axisymmetric portion of the interface treated as rigid. This change in the boundary condition on the surface of the sphere was an attempt to model a supported drop. The results for the case of a hemispherical liquid surface are the filled circles in figure 7. These frequencies are larger than those of the free half-drop, but still less than the experimental data. The natural frequencies from the theoretical work of Lyubimov *et al.* (2006) for the first three axisymmetric modes of a pinned hemispherical drop are shown in figure 7 with the filled diamonds. These compare well with the results from Strani & Sabetta (1984).

One possible reason for the lower theoretical frequencies compared to the experimental data is the hemispherical drop shape in the theory (a zero-gravity condition), whereas there is a small amount of drop flattening due to gravity as the drop volume increases in the experiments. However, the collapse of the experimental data into a single curve, as shown in figure 7 for $G < 2$, argues against this reason.

As the mode number increases, both the results of Strani & Sabetta (1984) and those of the free half-drop appear to approach the limiting case of axisymmetric, planar standing waves on the surface of a hemispherical drop (neglecting depth effects), which has the dispersion relation of $\omega_m^* = \sqrt{8}m^{3/2}$. The experimental data seem to

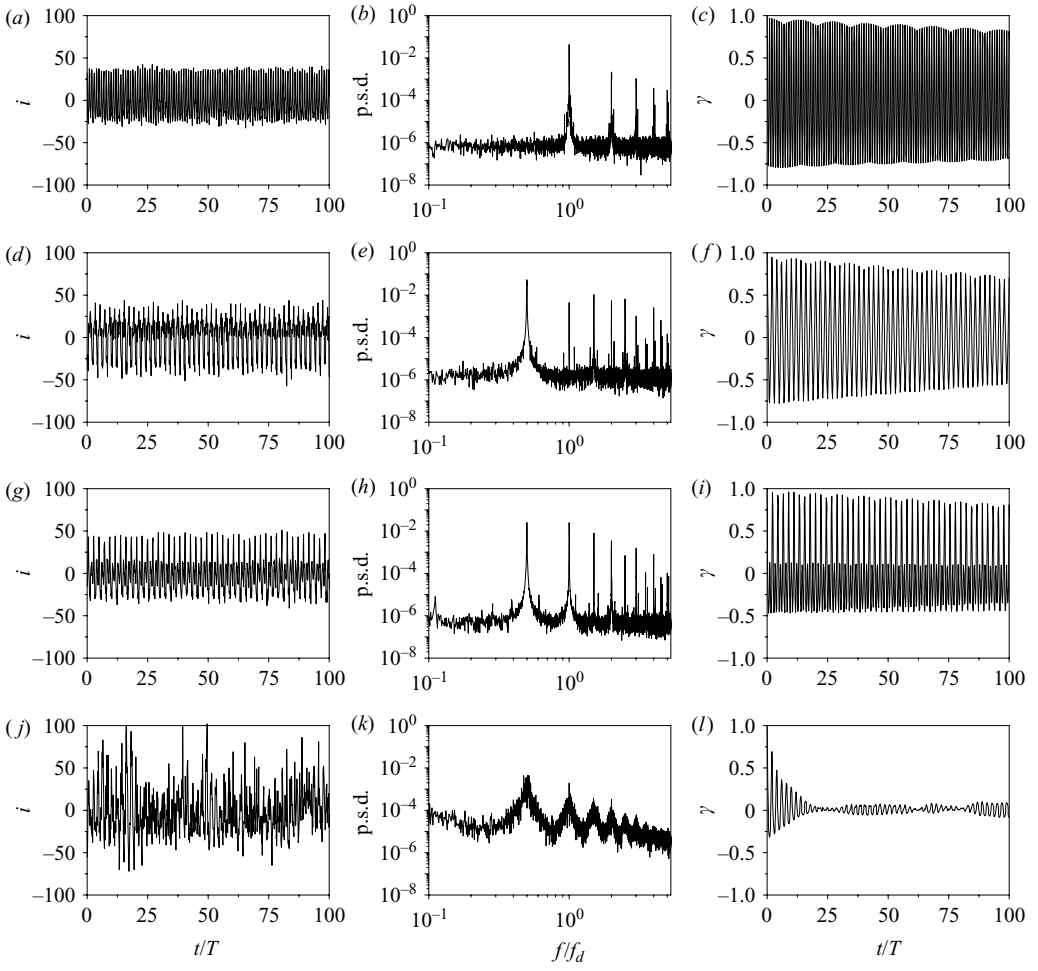

FIGURE 8. (a, d, g, j) The light intensity fluctuation $i(t/T)$, (b, e, h, k) the corresponding power spectrum $P(f/f_d)$, and (c, f, i, l) the corresponding autocorrelation function $\gamma(t/T)$. The dimensionless frequency $\omega_d^* = 159.6$ and $V^* = 1.77$ for all measurements. (a, b, c) The axisymmetric mode at $r/R_c = 0.6$ and $a^* = 13.3$, (d, e, f) azimuthal waves at $r/R_c = 0.93$ and $a^* = 42.0$, (g, h, i) the lattice mode at $r/R_c = 0.6$ and $a^* = 77.8$, and (j, k, l) the pre-ejection mode at $r/R_c = 0.6$ and $a^* = 275.0$.

approach this same power-law behaviour, but with a slightly higher frequency than the analytical results. Physically, this means that at high mode numbers, the qualitative response of the drop is less sensitive to the presence of the support.

The frequency content of the axisymmetric interface motion of the drop for any mode number m was determined from measurements of the light intensity $I(t)$ taken from the video image of a top view of the drop interface at a fixed radial location. The fluctuation of the light intensity is defined as $i(t) = I(t) - \overline{I}$, where $\overline{I}$ is the time-averaged intensity at this fixed location. As long as the motion is axisymmetric, $i(t)$ is representative of the entire interfacial motion up to a multiplicative constant.

Axisymmetric standing waves with $m = 13$ were forced in a 100 µl drop at an acceleration of $6.6g$ and a driving frequency of 903 Hz ($V^* = 1.77$, $a^* = 13.3$, $\omega_d^* = 159.6$). The fluctuation of the light intensity at $r = 0.6\,R_c$, where R_c is the contact

radius, is shown in figure 8(*a*). The corresponding power spectrum $P(f/f_d)$ and the normalized autocorrelation function $\gamma(\tau)$, defined as

$$\gamma(\tau) = \int_{-\infty}^{\infty} i(t)i(t+\tau)\,\mathrm{d}t \Big/ \int_{-\infty}^{\infty} i_m(t)i_m^*(t)\,\mathrm{d}t, \tag{3}$$

are given in figures 8(*b*) and 8(*c*), respectively. Both $i(t)$ and $\gamma(\tau)$ are shown for 100 driving periods T. The major content of the power spectrum occurred at the driving frequency f_d. The first four higher harmonics are one to two orders of magnitude lower. The power spectrum of the bare diaphragm also included spectral peaks at these harmonics. However, the first harmonic for the bare diaphragm was four to five orders of magnitude lower than the fundamental spectral component, even at the much higher forcing levels that typically lead to droplet ejection. Therefore, the higher harmonics measured on the drop interface were most probably generated by nonlinear wave interactions, rather than by nonlinear diaphragm motion. The slow decrease in the envelope of the autocorrelation function in figure 8(*c*) can be attributed to the presence of these higher harmonics and noise. As the forcing amplitude increases and approaches the acceleration threshold for the azimuthal instability ($a_a^* = 36.4$), the magnitudes of the higher harmonics in the wave motion also increase.

Further discussion of the spectral content of the interfacial motion for the azimuthal, lattice and pre-ejection modes, including the appearance of subharmonic motion in these modes is presented in § 3.3, 3.4 and 3.5, respectively.

3.3. *Azimuthal waves*

When the forcing amplitude was increased above $a_a = 18g$ for a 100 µl drop forced at $f_d = 903$ Hz ($a_a^* = 36.4$, $V^* = 1.77$, $\omega_d^* = 159.6$), an azimuthal instability of the drop interface was triggered along the contact line (figures 4*c* and 5*b*). The azimuthal waves were initially stationary, but as the forcing amplitude increased further, they began to rotate either clockwise or counterclockwise. Either direction was possible because of the rotational symmetry of the waves around the drop and the effect of small random perturbations in the system. Further increases in the forcing amplitude caused the azimuthal waves to propagate inward, until finally, when the forcing amplitude was about $a^* = 55$–60, the azimuthal waves were fully coupled to the axisymmetric waves and had spread to the top of the drop (figure 5*c*).

The fluctuation light intensity $i(t)$ from the interfacial motion associated with azimuthal waves is shown in figure 8(*d*) for the radial position $r = 0.93\,R_c$ (near the drop contact line) with the forcing conditions $a = 20.8g$ and $f_d = 903$ Hz ($a^* = 42.0$ and $\omega_d^* = 159.6$). The corresponding power spectrum $P(f/f_d)$ and autocorrelation function $\gamma(\tau/T)$ are shown in figures 8(*e*) and 8(*f*), respectively. The power spectrum and the autocorrelation function indicate that the dominant frequency of the azimuthal waves is the first subharmonic of the driving frequency $f_d/2$. Furthermore, the spectral peaks at integer multiples of $f_d/2$, which were not present in the power spectrum of the bare diaphragm, indicate the presence of nonlinear coupling between the subharmonic azimuthal waves and the axisymmetric waves at the fundamental frequency and its higher harmonics.

Although the azimuthal waves were initially triggered along the drop's circumference, the resultant subharmonic frequency response was detectable across the entire interface of the drop. This is demonstrated in figure 9 where the power spectra of the light intensity fluctuation at four radial locations on the drop are shown. The forcing conditions were the same as for figures 8(*d*)–8(*f*). The energy content of the interfacial motion was largest near the contact line (figure 9*a*) and decreased

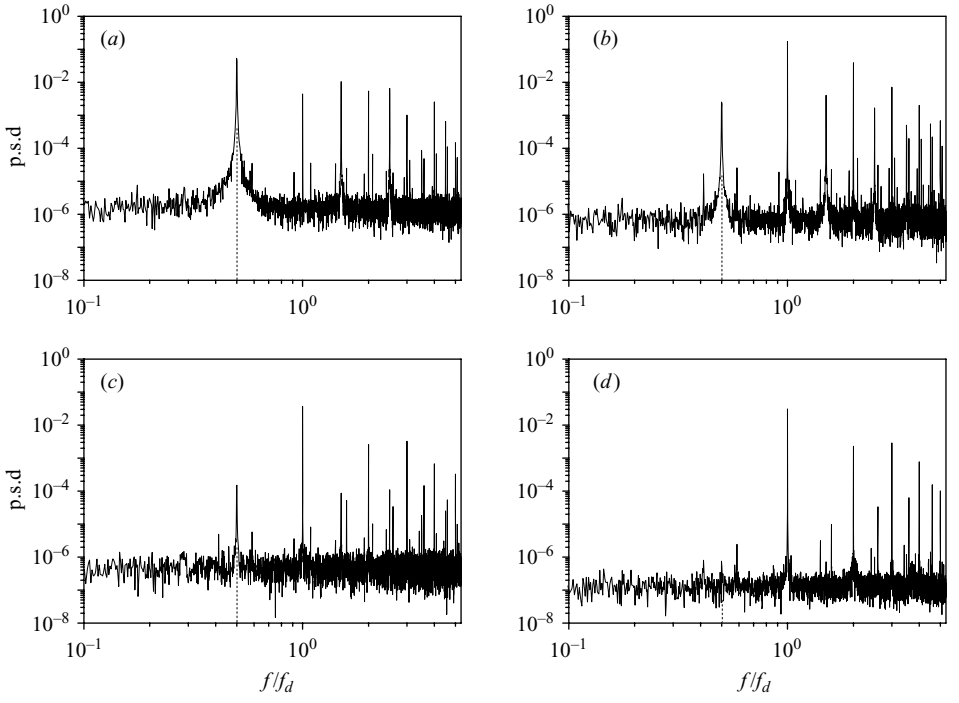

FIGURE 9. The power spectrum of the light intensity fluctuation $i(t/T)$ for azimuthal waves at (*a*) $r/R_c = 0.93$, (*b*) 0.75, (*c*) 0.5, and (*d*) 0.05. The dimensionless forcing frequency $\omega_d^* = 159.6$, $V^* = 1.77$ and the forcing acceleration $a^* = 42.0$, which are the same conditions as for the azimuthal waves shown in figures 8(*d*)–8(*f*). The subharmonic frequency is marked by the dotted line.

toward the centre of the drop (figure 9*b*–*d*). This indicates that the excited azimuthal instability mode was strongly amplified along the drop's circumference, but not near the centre of the drop.

The subharmonic frequency response of the drop suggests that the azimuthal wave instability is a parametrically driven instability similar to Faraday waves. Noblin *et al.* (2005) suggested that these azimuthal waves are the high-wavenumber analogue of the low-wavenumber subharmonic triplon modes that they studied in large flat liquid drops (puddles). However, in their experiments, the vibrating drop developed the triplon instability only after a transition from a pinned to a moving (oscillating) contact line. In the present experiments, the contact line appeared to stay pinned until the appearance of the azimuthal instability.

Threshold acceleration versus driving frequency data for the azimuthal instability are presented in figure 10 for a 100 µl water drop with the dimensionless volume $V^* = 1.77$. The measurement was done in three different ways: (i), (ii) fix the acceleration and perform an increasing and then a decreasing frequency sweep at a rate of $2\,\mathrm{Hz\,s^{-1}}$ (open triangles), and (iii) fix the driving frequency and increase the driving amplitude at a rate of $12g\,\mathrm{s^{-1}}$ (filled triangles). All of these measurements agree fairly well with each other. The results indicate that the threshold acceleration increases monotonically with the driving frequency.

There seems to be no analytical work on the azimuthal instability in a sessile drop available in the literature. The closest comparable work is the Faraday capillary-wave instability. The threshold acceleration for inviscid Faraday waves in a liquid layer

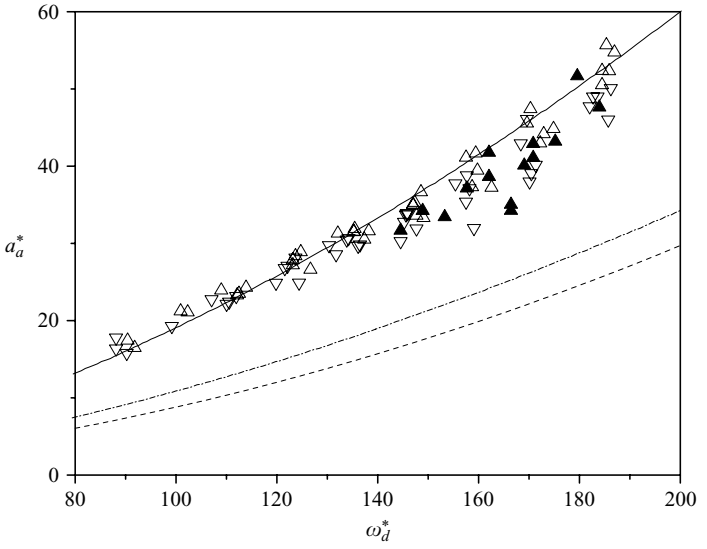

FIGURE 10. The threshold acceleration versus driving frequency for the onset of azimuthal waves in a 100 µl water drop ($V^* = 1.77$). Experimental data for: an increasing (△) and decreasing (▽) frequency sweep, an amplitude sweep (▲), the analytical result of Christiansen *et al.* (1995) $a_a^* = 4k_a^*\omega_d^*/Re$ (- - -), and Kumar's (1996) solutions for an equivalent viscous liquid layer of depth $h = 2.6$ mm (–·–) and 0.95 mm (—).

of finite depth is zero (Benjamin & Ursell 1954). Viscous damping effects cause the threshold acceleration to be non-zero, as shown by Miles (1984). Landau & Lifschitz (1987) computed the damping coefficient for gravity waves in a finite liquid layer by computing the viscous dissipation in the bulk liquid based on the potential-flow solution for the waves. The result was a damping coefficient $C = 2\nu k^2$. Christiansen *et al.* (1995) added a viscous damping term with this damping coefficient directly to the linearized disturbance equation for a finite liquid layer (Mathieu's equation). Their result for the threshold acceleration written in dimensionless form using the inviscid scales from the present paper and applied to the azimuthal waves is

$$a_a^* = \frac{4k_a^*\omega_d^*}{Re\tanh(k_a^*h^*)}. \tag{4}$$

For the wavenumbers observed in the azimuthal waves (see below) and any reasonable value for the drop thickness, $\tanh(k_a^*h^*) \approx 1$. This means that the capillary waves do not feel the bottom surface, i.e. they behave like deep-water capillary waves. This result is plotted (with $\tanh(k_a^*h^*) = 1$) as the dashed line in figure 10. The result underestimates the threshold acceleration for the drop by a factor of about two. Thus, bulk damping is probably not important with respect to the azimuthal wave instability of a forced sessile drop.

Besides viscous damping in the bulk liquid, there are three other sources of damping in the drop: a viscous boundary layer along the solid–liquid interface; capillary damping due to a moving contact line; and interfacial damping due to an interfacial boundary layer. The characteristic length scale for a viscous wall boundary layer in the present experiments is $l_v = (\nu/\omega)^{1/2}$. At its largest, $l_v < 0.02$ mm and $l_v/R < 0.01$. Thus, it is believed that the wall boundary layer away from the contact line does not contribute significantly to the overall damping.

The contribution of contact-line dynamics to the damping has started to become fully understood only recently (e.g. Lyubimov *et al.* 2006) following the pioneering work of Miles (1967, 1991) and Hocking (1987). Despite careful examination of the incipient azimuthal wave motion near the contact line in the present experiments, there is no conclusive evidence of significant macroscopic oscillatory motion of the contact line. If such motion existed, it was very small and obscured by the interfacial motion of the azimuthal waves near the contact line. Thus, damping due to a moving contact line is probably not important for azimuthal waves.

The last source of damping in the drop is an interfacial boundary layer caused by contamination of the interface, which is known to significantly increase damping rates (e.g. Henderson 1998). Distilled water was used in the present experiments and its purity and the possible contamination of the air/water interface were considered throughout the work because virtually no water is pure and free of contaminants. The most conservative estimate of the time required to contaminate a clean air/distilled-water interface was given by Henderson & Miles (1994). They estimated that contamination becomes important in about 5 min. Besides promoting non-contamination by following strict procedures in storing, cleaning and shielding experimental surfaces, it is also important to note that typical experiments in the present work were very short – most of them were under 1 min in duration owing to the high forcing frequencies used (hundreds of Hz). The data shown in figure 10 are worst-case examples with respect to surface contamination in the present work. Here, the duration of individual experiments was several minutes and different sets of data were collected on different days. Although there is some scatter in the data, no significant variation in the threshold acceleration for azimuthal waves is observed. This result precludes the effect of damping due to interfacial contamination and an interfacial boundary layer. Thus, the most likely cause for the higher threshold acceleration compared to that predicted by (4) is additional viscous damping in the contact-line region of the drop, a finite-thickness effect, and/or the compact geometry of the drop compared to the layer.

The scaling for the threshold acceleration in (4) can be obtained using the following argument. The threshold acceleration a_a must overcome the viscous damping in the system. Therefore, $a_a \sim VC$, where V is a typical velocity scale and C is the viscous damping coefficient with units of inverse seconds. For Faraday waves, the velocity scale depends on the forcing frequency and the wavenumber of the waves in the form $V \sim \omega_d/k_a$. The net result is

$$a_a \sim \frac{\omega_d C}{k_a}. \tag{5}$$

Substituting the damping coefficient for bulk viscosity used by Christiansen *et al.* (1995), $C = 2\nu k_a^2$, into (5) yields the scaling relation $a_a \sim k_a \omega_d \nu$. This is the same scaling as the dimensional form of (4). The $\tanh(k_a^* h^*)$ factor in (4) is a geometry effect and cannot be given by a scaling analysis.

A least-squares best fit to the data in figure 10 yielded the relation $a_a \sim \omega_d^{1.446}$. This does not match the linear scaling with frequency derived above from a bulk-liquid viscous damping coefficient, but it does suggest a frequency exponent of 3/2. Based on the idea that viscous effects determine the threshold acceleration, a scaling analysis was done assuming a frequency exponent of 3/2 and neglecting surface-tension effects. The result is $a_a \sim \omega_d^{3/2} \nu^{1/2}$. Substituting this into (5) gives the scaling for the viscous damping coefficient as $C \sim k_a (\omega_d \nu)^{1/2}$.

Kumar (1996) considered Faraday waves in a viscous liquid layer of finite depth by starting with the original governing equations including viscosity. The leading-order damping coefficient in the limit of small viscosity from his equation (5.2) is $C = 2k(\omega\nu)^{1/2}/\sinh(2kh)$. The scaling of this result agrees with the scaling for the experimental data. This gives support to the idea that viscous damping in the boundary layer along the solid boundary is responsible for the threshold acceleration of azimuthal waves in the forced drop. The only place where interfacial motion could produce a viscous boundary layer on the solid wall with a size comparable to the drop thickness is in the contact-line region where the drop is thinnest.

Kumar's result is plotted in figure 10 using the inviscid scales of this paper and a characteristic length scale of $h = 2.6$ mm, which is the mass-averaged depth of the drop. The curve is just above the Christiansen *et al.* (1995) result, and still underestimates the measured critical acceleration. In a planar layer 2.6 mm thick, interfacial motion does not produce much of a viscous wall boundary layer, bulk viscous damping is dominant, and so the result should be close to Christiansen *et al.*'s. For a planar liquid layer of thickness $h = 0.95$ mm, viscous wall damping becomes as important as bulk damping for the lower frequencies and the resultant curve passes through the experimental data. Comparing the liquid layer results to the drop results in this way is risky because of the different geometries of the interfaces in these two cases. However, the experimental data do suggest that the instability originates near the contact line (see figure 9 and the discussion above), which is the only place where a viscous wall boundary layer could be produced and have an effect on the interfacial motion. Thus, the agreement between the experimental data and Kumar's result for a layer thickness of 0.95 mm suggests that a viscous boundary layer near the contact line is important to the onset of the azimuthal instability in a forced sessile drop.

If the scaling analysis above is correct, the threshold acceleration depends on the viscosity as $\nu^{1/2}$. So, for example, increasing the fluid kinematic viscosity by a factor of ten would increase the threshold acceleration by a factor of $\sim$3.2. However, at such high forcing levels, the amplitude of the axisymmetric interfacial waves may be large enough to make them unstable to another mode of instability before the onset of the azimuthal instability. In an initial test with a glycerine/water solution whose viscosity was about twenty times that of pure water, the first observed instability occurred over the entire interface of the drop, i.e. the azimuthal instability along the contact line did not occur. Further work on the relationship between fluid viscosity and the threshold acceleration is discussed by Vukasinovic, Smith & Glezer (2007).

The dimensionless wavenumber of the azimuthal instability $k_a^* = 2\pi R/\lambda_a$, where λ_a is the wavelength of the unstable motion, was found by counting the number of azimuthal wave periods n_a around the contact line at the onset of the instability. The wavenumber is related to n_a by $k_a^* = n_a R/R_c$, where R_c is the measured contact radius of the drop. This result is presented as a function of the dimensionless frequency of the azimuthal instability $\omega_a^* = \omega_d^*/2$ in figure 11 for three drop volumes $V^* = 1.88$, 1.82 and 1.77 (50, 75, and 100 µl) with contact radii $R_c = 3.24$, 3.70 and 4.12 mm, respectively. For comparison, the well-known dispersion relation for inviscid capillary waves on a liquid layer of finite depth h is $\omega^2 = (\sigma/\rho)k^3 \tanh(kh)$ (Lighthill 1978). The smallest value of the dimensionless wavenumber from figure 11 is $k^* = 8$ for the 50 µl drop, which gives $k = 2.68\,\mathrm{mm}^{-1}$. As before, it is not clear what liquid depth is appropriate, but choosing $h = 0.95$ mm gives $\tanh(kh) = 0.988$. Therefore, the liquid-depth effect in the drop is negligible. The resulting dimensionless dispersion relation for inviscid deep-water capillary waves, $\omega_a^* = k_a^{*3/2}$, is plotted in figure 11. The results of Kumar (1996) for $h = 2.6$ mm and 0.95 mm are also presented in this figure. These

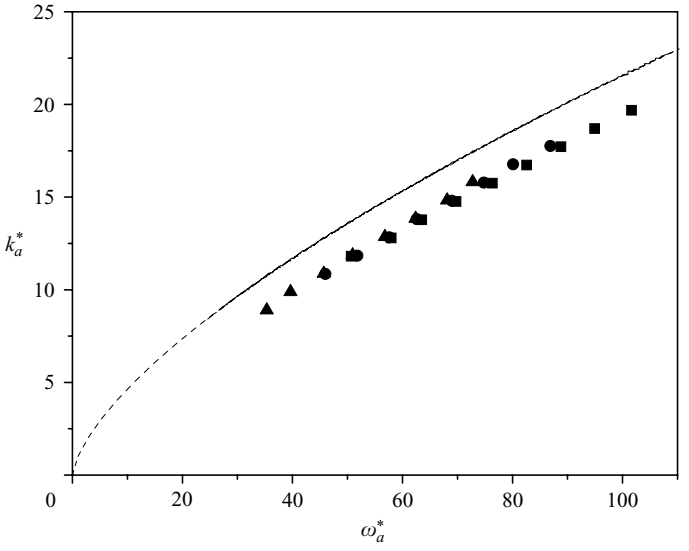

FIGURE 11. Variation of the dimensionless wavenumber k_a^* with the subharmonic frequency $\omega_a^* = \omega_d^*/2$ for azimuthal waves with drop volumes $V^* = 1.77$ (■), 1.82 (●), and 1.88 (▲). The deep-water capillary-wave dispersion relation (- - -) and Kumar's (1996) solutions for the equivalent viscous liquid layer of depth $h = 2.6$ mm (–·–) and 0.95 mm (—) lie on top of each other.

curves lie on top of the inviscid curve. The experimental wavenumbers are always smaller than those for inviscid deep-water capillary waves and Kumar's results at any given frequency. A least-squares power-law fit to the experimental wavenumbers yields an exponent of 1.34, about 10 % smaller than 1.5. In addition, it looks as if the slope of the experimental data for each drop volume is slightly different.

One explanation for the smaller experimental values of the wavenumber compared to the values from the inviscid dispersion relation for a given frequency is the effect of viscous dissipation increasing the wave length of the azimuthal waves. The fact that Kumar's results lie on top of the inviscid result indicates that bulk viscosity in a liquid layer of finite depth is not the source of this dissipation. Another possibility is the viscous boundary layer on the lower solid surface. The time scale for vorticity transport from the solid surface across a distance ℓ is $t_v = \ell^2/\nu$. Setting this time scale equal to the inertial time scale $1/\omega_a$ leads to the conclusion that in the worst case, the distance ℓ is two orders of magnitude smaller than the corresponding wavelength λ_a. Thus, viscous dissipation from the solid surface for a liquid layer is typically neglected. However, the previous discussion that viscous boundary-layer effects in the contact-line region of the sessile drop may affect the threshold acceleration of the azimuthal-wave instability implies that such effects could also influence the motion of azimuthal waves. Thus, viscous effects from the lower boundary near the contact line may be the explanation for the smaller wavenumbers of the azimuthal waves compared to deep-water capillary waves, as seen in figure 11.

A mechanism for the azimuthal instability is suggested by several of the observations discussed above. First, the interfacial displacement is significant along the contact line of the drop in the axisymmetric state just before onset of the azimuthal instability (figure 4*b*). Secondly, the origin of the subharmonic motion is near the contact line (figure 9). Finally, the wave length of the azimuthal mode closely follows the trend

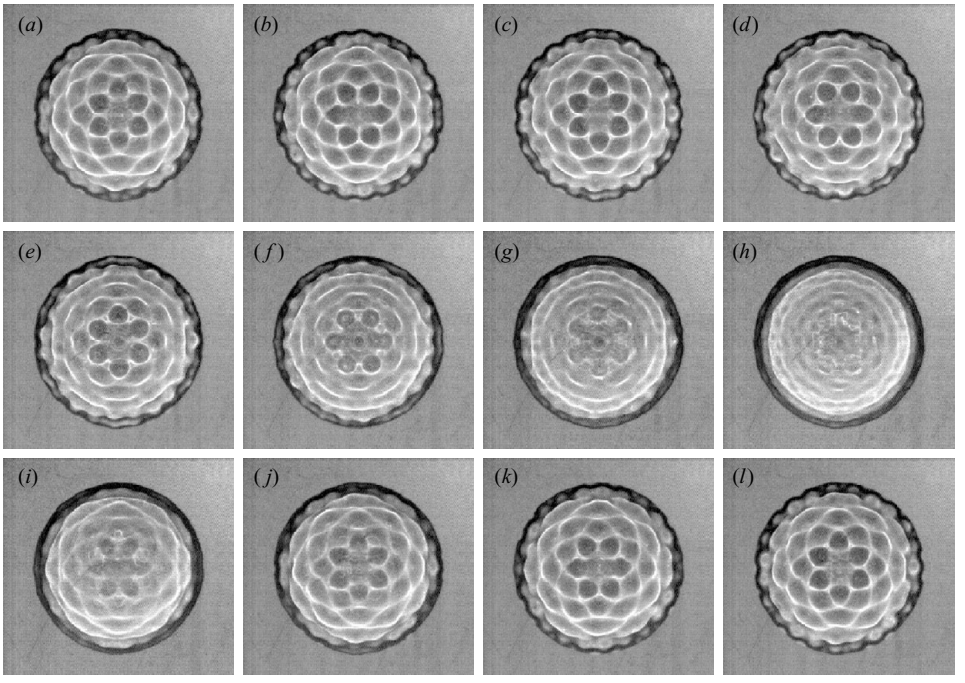

FIGURE 12. Time variation of the lattice mode in figure 5(*d*) at (*a*) $t/T = 0$, (*b*) 0.9, (*c*) 1.8, (*d*) 2.7, (*e*) 3.6, (*f*) 4.5, (*g*) 5.4, (*h*) 6.3 (*i*) 7.2, (*j*) 8.1, (*k*) 8.9, and (*l*) 9.9. Experimental conditions correspond to those of figure 5(*d*).

of Faraday capillary waves offset by some amount attributed to viscous damping (figure 11). These observations suggest that the instability is a Faraday capillary-wave instability of the axisymmetric base state owing to the radial motion of the interface near the contact line. The vertical motion of the support is translated to radial motion of the interface by the geometry of the sessile drop. The near-90° contact angle causes this radial motion to be nearly normal to the interface at the contact line. Thus, it is reasonable to suppose that the interface of the drop near the contact line will develop a Faraday instability to capillary waves.

It is also noteworthy that the triplon modes observed in large flat liquid drops by Noblin *et al.* (2005) are subharmonic (parametric with respect to the forcing) and that their dispersion relation scales as $\omega \sim k^{3/2}$; both of which agree with the observed azimuthal waves in the present work.

3.4. *The lattice mode*

Following the onset and spreading of the azimuthal instability, a new mode emerged in the form of a striking azimuthal lattice structure with a well-defined sixfold symmetry (figures 5*d* and 12). The onset forcing amplitude for this mode was $a_l = 38g$ at a forcing frequency of $f_d = 903$ Hz ($a_l^* = 76.8$ and $\omega_d^* = 159.6$). To the best of our knowledge, this wave pattern has not been reported previously in the literature. For the lattice mode to form, the wavenumbers for the axisymmetric waves and the azimuthal waves in the drop must attain a unique relationship to each other.

Once the lattice mode is fully developed, the wave pattern itself is time periodic. A sequence of high-speed video images captured at equal time increments of $0.9\,T$, where T is the fundamental driving period, is shown in figure 12. Each image exhibits

four to five adjacent circular azimuthal bands of increasing radius having an integer number of waves. The image sequence shows that the wave pattern in each band shifts azimuthally and, at the same time, the amplitudes of the azimuthal waves vary periodically. The period of the lattice mode from this image sequence is $9.9\,T$, which gives a modulation frequency of $0.1\,f_d$ (90.3 Hz).

Time traces of light intensity for the lattice mode were measured at $r/R_c = 0.6$ with drop forcing conditions of $a = 38.5g$ and $f_d = 903$ Hz ($a^* = 77.8$ and $\omega_d^* = 159.6$). The light intensity fluctuation $i(t)$, the corresponding power spectrum $P(f/f_d)$, and the autocorrelation function $\gamma(t/T)$ are shown in figures 8(*g*)–8(*i*), respectively. The power spectrum shows equally strong subharmonic and harmonic motions across the drop interface. There is a spectral peak in the power spectrum at $f \approx 0.11\,f_d$, which is close to the observed modulation frequency of the lattice pattern $f \approx 0.1\,f_d$. However, its power magnitude is significantly lower than the subharmonic and harmonic components of the motion (Figure 8*h*). The lattice pattern persisted in the drop until the forcing amplitude was increased to about $a \approx 55g$ ($a^* \approx 111$).

3.5. *Pre-ejection mode*

Once the symmetry of the lattice mode was broken (figure 5*e*) at a forcing amplitude of $a \approx 55g$, a more complex state appeared containing individual wave cells. These cells became more clearly defined as the forcing amplitude increased until the onset of droplet ejection at $a = 136g$ (figure 5*f*).

The light intensity measurements on the drop interface for the pre-ejection mode are shown in figures 8(*j*)–8(*l*) for $r/R_c = 0.6$, $a = 136g$, and $f_d = 903$ Hz ($a^* = 275.0$ and $\omega_d^* = 159.6$). The first subharmonic peak in the power spectrum (figure 8*k*) is now slightly larger than the harmonic peak. There is some broadening of all spectral peaks and a general increase in the low-frequency portion ($f/f_d < 0.5$) of the power spectrum, indicating increased disorder in the wave motion. Furthermore, the autocorrelation function (figure 8*l*) drops sharply within $20\,T$ (at the subharmonic frequency).

These observations are similar to observations from earlier Faraday-wave experiments (see the review by Miles & Henderson 1990, for other examples). This global, qualitative description of the localized interface motion is also in accord with results from the non-optical measurements of Faraday waves reported by Cabeza *et al.* (2000). However, in contrast to the classic Faraday-wave experiment, the dominant subharmonic motion in the pre-ejection mode of the forced drop is preceded by multiple transitions associated with the geometry of the sessile drop and the small-displacement-amplitude high-frequency forcing used in this work. Similarly, Douady (1990) showed that when the liquid layer in a Faraday-wave experiment is not perfectly flat, harmonic waves generated by the meniscus at the boundary interfere and compete with the parametric waves. In the present experiments, harmonic motion is present in the wave dynamics at all times, while the energy content of the subharmonic motion appears with the azimuthal wave instability and progressively increases as the forcing acceleration increases. The complex dynamics seen on the interface of the forced drop and the drop's ultimate breakup are governed by the nonlinear interactions between the forced harmonic motion and the parametrically driven subharmonic motion.

4. Low-dimensional description of the temporal disorder

To further characterize the interfacial motion prior to the onset of droplet ejection, the light intensity from a point on the interface of the drop was measured phase-locked to the driving signal. Phase-locked measurements attenuate the effect of

frequencies higher than the driving frequency, including higher harmonics, and therefore emphasize the effect of the driving frequency on the interfacial motion. The resulting data are presented using a polar plot of light intensity versus phase of the driving signal, which is called a phase-orbit plot.

The measurements were done as follows. The frequency of the driving signal to the drop was set to 1000 Hz. The amplitude of the signal was slowly ramped to a prescribed level and then held fixed for approximately 5 s to ensure that the desired interfacial mode shape was fully established and periodic. The sampling rate of the video camera was set to 10 000 f.p.s., providing ten measurements per driving period or one measurement every 36° of phase in the driving signal. The light intensity from the radial locations corresponding to figure 8 was sampled for 0.8 s ($800\,T$) following the establishment of the interfacial motion.

Figure 13 shows six phase-orbit plots corresponding to axisymmetric waves, azimuthal waves, the lattice mode and the pre-ejection mode. These modes are visualized in figure 5(*a*, *b*, *d*, *f*) with a slightly lower frequency. The phase orbit for axisymmetric waves (figure 13*a*) is a single-loop closed orbit indicating harmonic motion of the waves. The overlapping of the orbits during 800 periods of the driving signal shows that there is little change in phase of the interfacial motion relative to the driving signal during this time interval.

The phase orbit for azimuthal waves just after onset is shown in figure 13(*b*). The two loops in the orbit are formed over a period of $2\,T$ indicating period doubling due to the subharmonic motion present on the interface. The overlapping of these double-loop orbits shows that the phase of the interfacial motion relative to the driving signal stays relatively fixed, and that there is little change in the phase difference between the subharmonic and harmonic motions on the interface of the drop.

The phase orbit for the lattice mode (figure 13*c*) is much thicker than the phase orbit for azimuthal waves. The underlying double-loop orbit is still present as shown in the phase orbit of figure 13(*e*), which represents only six consecutive periods of motion. The thickening of the orbit is due to a continuous loss in the phase coherence of the motion. The double loops nearly coincide over consecutive periods of the driving signal, but a slight shift in the phase occurs over time. There are no sharp changes in the relative phase between the subharmonic and harmonic motions, but the overall phase coherence with the driving signal is weakly disrupted. The underlying structure of the motion for the lattice mode, not captured in figure 13(*c*), will be described below.

Figure 13(*d*) shows the phase-orbit plot for the pre-ejection mode. The underlying double-loop orbit is still present, as seen in figure 13(*f*) showing data for only six consecutive driving periods, but a distinguishable loss of coherence is visible between the subharmonic and harmonic motions after each consecutive driving period. Overall, the thick annular region covered by the phase orbit over a time period of $800\,T$ in figure 13(*d*) indicates that there is virtually no phase coherence between the interfacial motion and the driving signal.

An easier way to see the existence of phase coherence, or lack thereof, in a phase-locked data set is to display the data in a phase-cut plot. A phase cut is a subset of the original phase-locked data taken at a particular phase ϕ_0 in the phase orbit for every period T of the original data. The resulting data I_i, where i is the index of the period, are plotted as the (x, y)-point (I_i, I_{i+1}) for all periods i.

The phase-cut plots (with $\phi_0 = 72°$) corresponding to the phase orbits from figure 13 are presented in Figure 14. The values corresponding to odd and even driving periods are marked in filled and open symbols, respectively. For axisymmetric waves

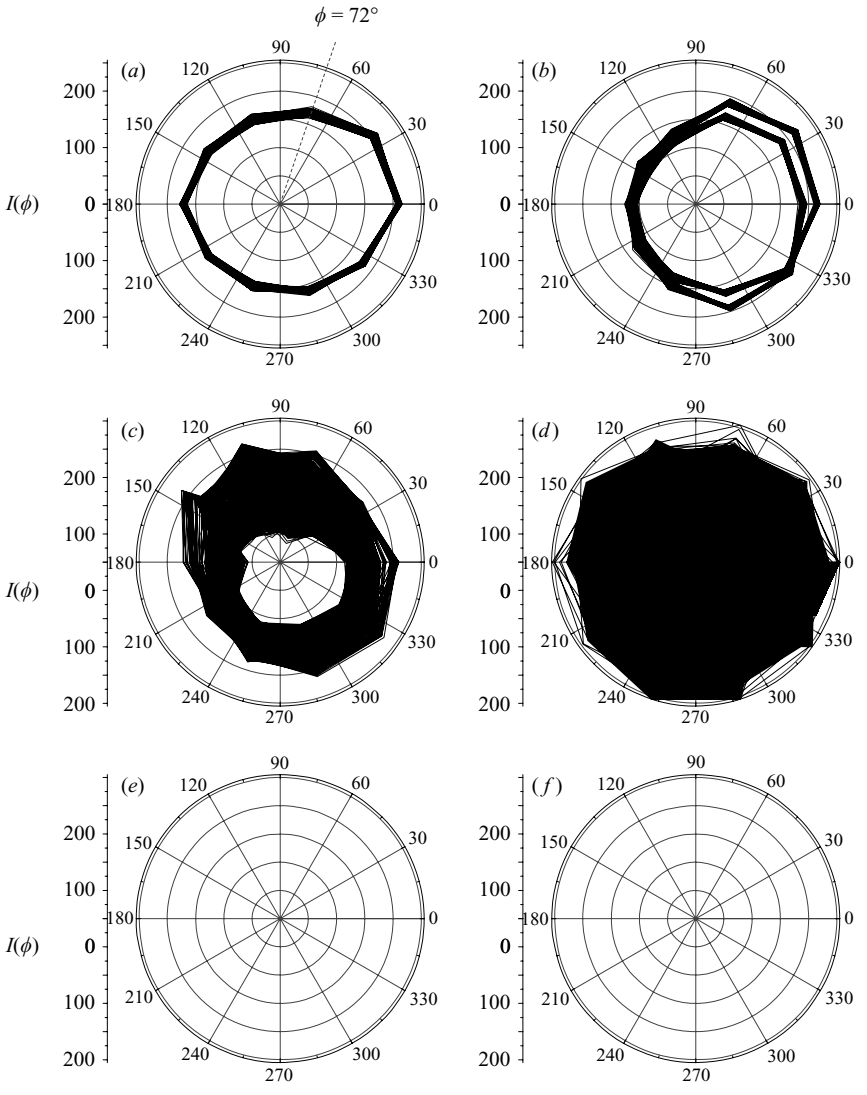

FIGURE 13. The variation in the light intensity I with respect to the phase ϕ of the driving signal from a drop with volume $V^* = 1.77$ (100 µl) at a driving frequency $\omega_d^* = 176.7$: (*a*) axisymmetric waves ($a^* = 37.8$, $r/R_c = 0.6$), (*b*) azimuthal waves ($a^* = 55.2$, $r/R_c = 0.93$), (*c*) lattice mode ($a^* = 104.7$, $r/R_c = 0.6$), and (*d*) pre-ejection mode ($a^* = 284.9$, $r/R_c = 0.6$). The variation of the light intensity during six consecutive driving periods is shown in (*e*) for the lattice mode and (*f*) for the pre-ejection mode.

(figure 14*a*), there is one small cluster of points containing both odd and even driving periods. This indicates harmonic motion with good phase coherence. The phase-cut plot for azimuthal waves (figure 14*b*) shows two tight clusters of points, one for odd periods and one for even periods. This means that the interfacial motion on the drop contains both harmonic and subharmonic components and that both components have good phase coherence.

The only way any conclusions could be drawn from the phase-orbit plot for the lattice mode (figure 13*c*) and the pre-ejection mode (figure 13*d*) was to view the

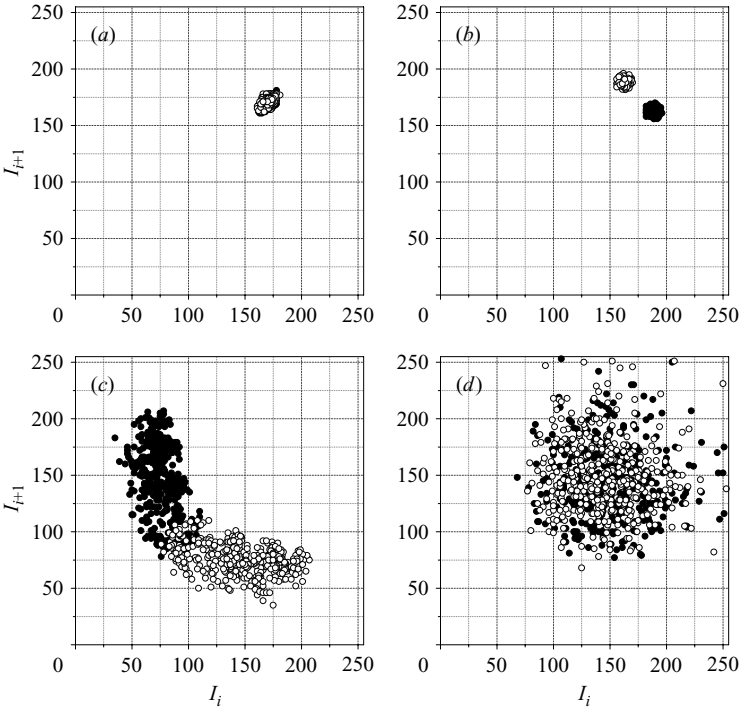

FIGURE 14. Phase-cut plots of the light intensity I at odd (●) and even (○) periods of the driving signal at $\phi_0 = 72°$; (a–d) correspond to the states in figure 13(a–d) respectively.

data for only a few periods (figure 13e, f). Figure 14(c) shows the phase-cut plot for the lattice mode. Here, the odd and even periods each have a distinct cluster that overlap slightly. The two clusters show that the underlying interfacial motion still has a distinct subharmonic component. The larger size of both clusters compared to those from figures 14(a, b) indicates a loss of phase coherence for the lattice mode. The phase-cut plot for the pre-ejection mode (figure 14d) shows only one large cluster containing both odd and even modes. This plot confirms the complete loss of phase coherence in the interfacial motion for the pre-ejection mode that precedes interface breakup.

5. Conclusions

The present investigation examined the evolution of interfacial waves on a sessile water drop forced to vibrate vertically at frequencies from zero to about 1 kHz by an underlying piezoelectric transducer. The motion of the diaphragm supporting the drop applied a radially varying acceleration field to the drop. The largest variation in acceleration, which occurred for the largest drop, was 15 % between the centreline and the contact line of the drop.

The drop was small enough to be close to the shape of a spherical-cap drop. For the largest drop, gravity flattened the drop so that the measured radius of the contact line was 8 % larger than the contact radius of a spherical-cap drop with the same volume and contact angle. The spreading was less than 9 % for the smaller drops. Although

gravity did cause the static drop shape to spread out, there was no discernible effect of gravity on the dynamical drop motion seen in this work.

When the driving amplitude was slowly increased from zero, the drop exhibited the following sequence of motions: axisymmetric standing waves that were present with the smallest driving amplitude; the onset of azimuthal waves at the contact line; fully coupled azimuthal and axisymmetric waves; the lattice mode; a disordered pre-ejection mode; and finally, droplet ejection from individual wave cells. Of particular interest were three primary transitions: from axisymmetric standing waves to azimuthal waves, the appearance of the newly observed lattice mode, and the appearance of the disordered pre-ejection state.

The drop dynamics in this problem was nearly inviscid. The viscous boundary layer on the diaphragm was very small compared to the drop radius. Although distilled water was used for the drop, an interfacial boundary layer on the drop owing to the effects of interfacial contamination was not present owing to careful experimental procedures and the short duration of each experimental run, typically less than 1 min. Therefore, the only sources of damping in this system were viscous effects in the bulk liquid, viscous boundary-layer effects near the contact line, and contact-line dynamics. However, contact-line dynamics only became important for the higher values of the forcing acceleration, which released the pinned contact line from the solid surface of the diaphragm.

The forced axisymmetric standing waves in the drop were harmonic with the driving frequency and stayed relatively phase-locked to the motion of the diaphragm. A discrete set of axisymmetric resonance modes were recorded with mode numbers $m = 1$–14. The resonance frequencies scaled with the same capillary time scale used for an isolated drop, i.e. $\omega_m \sim \sqrt{\sigma/\rho R^3}$, where R is the radius of curvature of a spherical-cap drop with the same volume and contact angle. The dimensionless resonance frequencies depended only on the mode number. Contact-angle and gravity effects were negligible for the drop sizes investigated ($<100\,\mu$l). No macrosopic motion of the contact line was observed at any acceleration amplitude for this mode. Thus, it appeared that the contact line remained pinned at all times.

Azimuthal waves appeared around the contact line of the drop when the driving acceleration exceeded a well-defined critical level. They were subharmonic to the driving frequency and remained relatively phase locked to the motion of the diaphragm. The critical acceleration and wavenumber for this parametrically driven instability were compared to those for finite-depth, capillary Faraday waves with viscous dissipation as computed by Kumar (1996) and Christiansen *et al.* (1995). The critical wavenumbers for the azimuthal waves were consistently lower than those for Faraday waves, and the critical accelerations were consistently higher. These results suggest that viscous dissipation is stronger for azimuthal waves.

One possible source for this increased damping is contact-line dynamics. The contact line appeared to be pinned during the axisymmetric drop motion, but it was not possible to verify contact-line oscillations, or the lack thereof, during the onset of azimuthal waves. Another possible source for this increased dissipation could be the viscous boundary layer at the solid–liquid interface near the contact line. This boundary layer has a negligible effect on finite-depth Faraday waves in a liquid layer because it is far enough away from the wave motion at the interface. However, for azimuthal waves in a drop, the solid surface intersects the contact line of the drop, and so the viscous boundary layer could contribute to the dissipation of the wave motion in this region. Some evidence for this idea was observed in a preliminary experiment with a water/glycerine mixture. For a fluid mixture with a viscosity about

twenty times that of pure water, the azimuthal instability at the contact line was completely suppressed. The first observed instability in this case occurred over the entire interface of the drop.

The data presented in this work suggest a possible mechanism for the azimuthal instability. The geometry of the sessile drop converts the vertical vibration of the diaphragm to a significant radial motion of the interface near the contact line. This radial motion, which is approximately normal to the interface for contact angles near 90°, as seen in these small drops, undergoes a Faraday capillary-wave instability.

It is worth noting that the azimuthal instability seen in the present work is similar to the triplon modes in vertically vibrated liquid puddles reported by Noblin *et al.* (2005). Both instabilities are subharmonic with a dispersion relation that scales as $\omega \sim k^{3/2}$, the same as for capillary Faraday waves.

Increasing the driving amplitude still further caused the azimuthal waves to spread toward the centre of the drop. Above another clear threshold acceleration level, a striking lattice mode emerged. To our knowledge, this is the first time that such a mode has been observed in a forced sessile drop. The lattice mode is characterized by equally strong subharmonic and harmonic motions. The phase of the lattice mode does not stay locked to the motion of the diaphragm.

Further increases in the driving amplitude destroyed the lattice mode and brought the drop motion to a more disordered state with well-defined wave cells covering the interface of the drop. This state, called the pre-ejection mode, existed until the driving amplitude reached another threshold level. At this point, the wave amplitude of individual wave cells became large enough to start ejecting small droplets from the crest of the wave in the cell. The dominant frequency of the pre-ejection mode was subharmonic to the driving frequency and the phase showed no coherence with the motion of the diaphragm. The emergence of this subharmonic-dominant wave pattern suggests that the pre-ejection mode would also be the normal end state for Faraday waves in a highly forced liquid layer.

In summary, this work has produced new fluid dynamical observations involving the dynamics of a vertically vibrated sessile drop. The new phenomena are the result of a parametrically driven instability of the forced axisymmetric waves in the drop, which produce new non-equilibrium wave patterns on the interface of the drop.

The authors wish to thank Dr Arne Pearlstein and Dr Michael Schatz for insightful discussions and useful suggestions during the course of this investigation. This work was supported by NASA Microgravity Research Division, Grant NAG3-1949.

REFERENCES

Basaran, O. A. 1992 Nonlinear oscillations of viscous liquid drops. *J. Fluid Mech.* **241**, 169–198.

Basaran, O. A. & DePaoli, D. W. 1994 Nonlinear oscillations of pendant drops. *Phys. Fluids* **6**, 2923–2943.

Benjamin, T. B. & Ursell, F. 1954 The stability of the plane free surface of a liquid in vertical periodic motion. *Proc. R. Soc. Lond.* A **225**, 505–515.

Besson, T., Edwards, W. S. & Tuckerman, L. S. 1996 Two-frequency parametric excitation of surface waves. *Phys. Rev.* E **54**, 507–513.

Cabeza, C., Negreira, C., Schifino, A. C. & Gibiat, V. 2000 Experimental determination of point localized time correlation and power spectrum in a Faraday experiment. *Intl J. Bifur. Chaos* **10**, 2233–2244.

Christiansen, B., Alstrøm, P. & Levinsen, M. T. 1995 Dissipation and ordering in capillary waves at high aspect ratios. *J. Fluid Mech.* **291**, 323–341.

Crum, L. A. & Roy, R. A. 1994 Sonoluminescence. *Science*, **266**, 233–234.

DePaoli, D. W., Feng, J. Q., Basaran, O. A. & Scott, T. C. 1995 Hysteresis in forced oscillations of pendant drops. *Phys. Fluids* **7**, 1181–1183.

Douady, S. 1990 Experimental study of the Faraday instability. *J. Fluid Mech.* **221**, 383–409.

Edwards, W. S. & Fauve, S. 1994 Patterns and quasi-patterns in the Faraday experiment. *J. Fluid Mech.* **278**, 123–148.

Faraday, M. 1831 On a peculiar class of acoustical figures, and on certain forms assumed by groups of particles upon vibrating elastic surfaces. *Phil. Trans. R. Soc. Lond.* **121**, 299–340.

Gañán, A. & Barrero, A. 1990 Free oscillations of liquid captive drops. *Microgravity Sci. Technol.* **3**, 70–86.

Gluckman, B. J., Arnold, C. B. & Gollub, J. P. 1995 Statistical studies of chaotic wave patterns. *Phys. Rev.* E **51**, 1128–1147.

Gollub, J. P. & Langer, J. S. 1999 Pattern formation in nonequilibrium physics. *Rev. Mod. Phys.* **71**, 396–403.

Henderson, D. M. 1998 Effects of surfactants on Faraday-wave dynamics. *J. Fluid Mech.* **365**, 89–107.

Henderson, D. M. & Miles, J. W. 1994 Surface-wave damping in a circular cylinder with a fixed contact line. *J. Fluid Mech.* **275**, 285–299.

Hocking, L. M. 1987 The damping of capillary–gravity waves at a rigid boundary. *J. Fluid Mech.* **179**, 253–266.

James, A., Vukasinovic, B., Smith, M. K. & Glezer, A. 2003*a* Vibration-induced drop atomization and bursting. *J. Fluid Mech.* **476**, 1–28.

James, A., Smith, M. K. & Glezer, A. 2003*b* Vibration-induced drop atomization and the numerical simulation of low-frequency single-droplet ejection. *J. Fluid Mech.* **476**, 29–62.

Kumar, K. 1996 Linear theory of Faraday instability in viscous liquids. *Proc. R. Soc. Lond.* A **452**, 1113–1126.

Lamb, H. 1932 *Hydrodynamics*. Cambridge University Press.

Landau, L. & Lifshitz, E. M. 1987 *Fluid Mechanics*. 2nd edn, Pergamon.

Lee, C. P., Anilkumar, A. V. & Wang, T. G. 1991 Static shape and instability of an acoustically levitated drop. *Phys. Fluids* **3**, 2497–2515.

Leissa, A. W. & Chern, Y. T. 1992 Approximate analysis of the forced vibration response of plates. *J. Vib. Acousts Trans. ASME* **114**, 106–111.

Lighthill, M. J. 1978 *Waves in Fluids*. Cambridge University Press.

Lundgren, T. S. & Mansour, N. N. 1988 Oscillations of drops in zero gravity with weak viscous effects. *J. Fluid Mech.* **194**, 479–510.

Lyubimov, D. V., Lyubimova, T. P. & Shklyaev, S. V. 2006 Behaviour of a drop on an oscillating solid plate. *Phys. Fluids* **18**, 012101.

Mesquita, O. N., Kane, S. & Gollub, J. P. 1992 Transport by capillary waves: fluctuating Stokes drift. *Phys. Rev.* A **45**, 3700–3705.

Miles, J. W. 1967 Surface-wave damping in closed basins. *Proc. R. Soc. Lond.* A **297**, 459–475.

Miles, J. W. 1984 Nonlinear Faraday resonance. *J. Fluid Mech.* **146**, 285–302.

Miles, J. W. 1991 The capillary boundary layer for standing waves. *J. Fluid Mech.* **222**, 197–205.

Miles, J. & Henderson, D. 1990 Parametrically forced surface waves. *Annu. Rev. Fluid Mech.* **22**, 143–165.

Noblin, X., Buguin, A. & Brochard-Wyart, F. 2004 Vibrated sessile drops: transition between pinned and mobile contact line oscillations. *Eur. Phys. J.* E **14**, 395–404.

Noblin, X., Buguin, A. & Brochard-Wyart, F. 2005 Triplon modes of puddles. *Phys. Rev. Lett.* **94**, 166102.

Perlin, M. & Schultz, W. W. 2000 Capillary effects on surface waves. *Annu. Rev. Fluid Mech.* **32**, 241–274.

Pratt, W. K. 1978 *Digital Image Processing*. John Wiley.

Prosperetti, A. 1980 Free oscillations of drops and bubbles: the initial-value problem. *J. Fluid Mech.* **100**, 333–347.

Prosperetti, A. & Oguz, H. N. 1993 Impact of drops on liquid surfaces and the underwater noise of rain. *Annu. Rev. Fluid Mech.* **25**, 577–602.

Range, K., Smith, M. K., & Glezer, A. 1998 An experimental investigation of vibration-induced single droplet ejection. *Fifty-First Meeting of the American Physical Society – Division of Fluid Dynamics, Philadelphia, PA, November 22–24.*

Rayleigh, Lord 1879 On the capillary phenomena of jets. *Proc. R. Soc. Lond.* A **29**, 71–97.

Rodot, H., Bisch, C. & Lasek, A. 1979 Zero-gravity simulation of liquids in contact with a solid surface. *Acta Astronaut.* **6**, 1083–1092.

Siekmann, J. & Schilling, U. 1989 On the vibrations of an inviscid liquid droplet contacting a solid wall in a low-gravity environment. *Appl. Microgravity Technol.* **2**, 17–26.

Simonelli, F. & Gollub, J. P. 1989 Surface wave mode interactions: effects of symmetry and degeneracy. *J. Fluid Mech.* **199**, 471–494.

Strani, M. & Sabetta, F. 1984 Free vibrations of a drop in partial contact with a solid support. *J. Fluid Mech.* **141**, 233–247.

Strani, M. & Sabetta, F. 1988 Viscous oscillations of a supported drop in an immiscible fluid. *J. Fluid Mech.* **189**, 397–421.

Trinh, E. & Wang, T. G. 1982 Large-amplitude free and driven drop-shape oscillations: experimental observations. *J. Fluid Mech.* **122**, 315–338.

Trinh, E., Zwern, A. & Wang, T. G. 1982 An experimental study of small-amplitude drop oscillations in immiscible liquid systems. *J. Fluid Mech.* **115**, 453–474.

Tsamopoulos, J. H. & Brown, R. A. 1983 Nonlinear oscillations of inviscid drops and bubbles. *J. Fluid Mech.* **127**, 519–537.

Vukasinovic, B. 2002 Vibration-induced droplet atomization. PhD thesis, Georgia Institute of Technology.

Vukasinovic, B., Smith, M. K. & Glezer, A. 2007 Mechanisms of free-surface breakup in vibration-induced liquid atomization. *Phys. Fluids* **19**, 012104.

Wilkes, E. D. & Basaran, O. A. 1997 Forced oscillations of pendant (sessile) drops. *Phys. Fluids* **9**, 1512–1528.

Wilkes, E. D. & Basaran, O. A. 1999 Hysteretic response of supported drops during forced oscillations. *J. Fluid Mech.* **393**, 333–356.